Mechanics of Materials 159 (2021) 103892

Contents lists available at ScienceDirect

Mechanics of Materials

journal homepage: www.elsevier.com/locate/mecmat

Research paper

Constrained Voronoi models for interpreting surface microstructural measurements

Sriram Ganesan [a], Iman Javaheri [a,b], Veera Sundararaghavan [a,*]

[a] Department of Aerospace Engineering, University of Michigan, Ann Arbor, MI, 48109, USA
[b] NASA Langley Research Center, Hampton, VA, 23681, USA

ARTICLE INFO

Keywords:
Microstructure reconstruction
Voronoi tessellation
Digital image correlation
Crystal plasticity
Slip systems

ABSTRACT

Measurement and analysis of microstructures is an essential aspect of materials design and structural performance. In the case of surface experimental measurements such as digital image correlation (DIC), it is beneficial to know the subsurface microstructure to interpret the surface observations accurately. However, subsurface microstructures are expensive to obtain through three-dimensional (3D) tomography. Hence, it is of interest to generate these structures computationally. In this work, a generalized inverse Voronoi problem is used to grow an approximate representation of the 3D microstructure from a surface electron backscatter diffraction (EBSD) image. The novelty of the approach is that the surface microstructure is retained during the simulation. This technique is employed for the reconstruction of a recrystallized magnesium alloy microstructure. Crystal plasticity finite element modeling (CPFEM) was employed for comparing the predicted surface strains in the reconstructed 3D microstructures against experimentally measured data. It is observed that the surface strains of different 3D reconstructions are qualitatively similar to the experiment. However, strong basal slip activation in some subsurface grains can influence the choice of activated slip systems on surface microstructures. The results show the implications of performing a full 3D crystal plasticity analysis of measured surface data as compared to only analyzing a two-dimensional extruded microstructure.

1. Introduction

Microstructure reconstruction is growing to be an important topic of interest in the field of materials modeling, simulation, and design (Bargmann et al., 2018). Voronoi diagram (also known as Dirichlet tessellation or Thiessen tessellation) is a popular tool for constructing polycrystalline microstructures of metallic alloys (Quey et al., 2011; Brahme et al., 2006). Voronoi tessellation and its dual, Delaunay triangulation are often used to describe observed structures in crystallography. A historical perspective for the development of the Voronoi diagram, including its implementations in crystallography along with the recent applications in a wide variety of fields, is provided in Okabe (1992). Voronoi tessellation essentially consists of partitioning a plane into polygons whose boundaries are defined based on a set of nodes called generator points. Given these generators, the Voronoi polygons can be constructed using the algorithm described in Evans and Jones (1987). For a two-dimensional (2D) micrograph, the Voronoi diagram is similar to a planar straight-line graph (PSLG) in which every polygon consists of the nodes that are closer to its corresponding generator point. The problem of obtaining these generators from the microstructure, referred to as the inverse Voronoi problem (IVP), has been well studied in Aurenhammer (1987), Evans and Jones (1987), Schoenberg et al. (2003). While the IVP is limited to finding one generator point for every grain, its variant, generalized inverse Voronoi problem (GIVP), has been used to represent every polygon with multiple generators (Trinchet-Almaguer and Pérez-Rosés, 2007). Such an approach is also followed in this paper. The properties of a GIVP for a simple case of rectangular tessellation is studied in Banerjee et al. (2013), where a method to find the minimal required number of generator points is described. Additionally, there are various measures used to describe deviation of grains from fully convex shapes. A measure for concavity or convexity of the grains, referred to as percentile average relative indented surface (PARIS) factor, is introduced in Panozzo and Hurlimann (1983). The PARIS factor quantifies the difference between the actual perimeter of the grain and the perimeter of its respective convex hull, relative to the convex hull. Additionally in Heilbronner and Keulen (2006), the area difference ratio between the original shape and its convex envelope is captured by a descriptor, denoted as $deltA$, for analyzing faults in rocks. It is to be noted that contrary to the PARIS factor, $deltA$ is sensitive to the tightness of the indenting angles. For very small angles such as a crack-tip or a propagating deformation

* Corresponding author.
E-mail addresses: sriramg@umich.edu (S. Ganesan), imanajv@umich.edu (I. Javaheri), veeras@umich.edu (V. Sundararaghavan).

https://doi.org/10.1016/j.mechmat.2021.103892
Received 6 January 2020; Received in revised form 18 January 2021; Accepted 19 April 2021
Available online 18 May 2021

twin within a grain, $deltA$ approaches 0%, while the PARIS factor may remain significantly larger.

Kinematic measurements at the microstructural scale are performed using atomic force microscopy (AFM) or scanning electron microscopy (SEM). These imaging methods allow for the mapping of strain fields at the surface of polycrystals with high spatial resolutions (Sutton et al., 2007). However, in the case of surface experimental measurements such as digital image correlation (DIC), it is important to know the subsurface effects to interpret the surface observations more accurately (Nicolas et al., 2019). Yet, subsurface information is expensive to obtain via non-destructive 3D tomography methods such as diffraction contrast tomography (DCT) and high-energy X-ray diffraction microscopy (HEDM) as well as destructive methods such as serial sectioning, which can only provide post-deformation data. Hence, it is of interest to numerically generate initial microstructures for computational modeling. Previously, for a better interpretation of surface experimental techniques such as DIC and orientation imaging microscopy (OIM), three-dimensional (3D) finite element modeling has been employed by using columnar grains (Bhattacharyya et al., 2001). Alternatively, in Brahme et al. (2006), the grains are approximated as a set of optimally packed ellipsoids, and the 3D microstructure is obtained by transferring the crystallized structure to a Voronoi tessellation. Morphological models are also developed for 3D concrete microstructures using multi-scale Poisson polyhedra in Escoda et al. (2015).

Recently, several methods based on geometric and feature matching algorithms (Groeber and Jackson, 2014; Jiao and Chawla, 2014; Bostanabad et al., 2016; Sundararaghavan, 2014; Javaheri and Sundararaghavan, 2020) have been developed to reconstruct 3D microstructures. However, when these methods generate the 3D microstructures, the surface microstructural information is not retained. An alternative approach used in this paper, is to construct the 3D microstructure using Voronoi sampling in the third dimension while maintaining the experimental surface image. The microstructure of interest in this paper underwent dynamic recrystallization, resulting in fairly equiaxed microstructures with a convex topology (Ganesan et al., 2021; Githens et al., 2020). As a result, the original surface SEM microstructure is first convexified, where internal twinned facets are removed from the 2D micrograph. Several sub-sections of a large representative EBSD map are then randomly extracted and successively stacked beneath the convexified 2D measurement. This is followed by perturbation of the Voronoi generators in the stacking direction using a normal random distribution. The resulting 3D structure is convexified once again to remove any artifacts penetrating onto the measured 2D surface. This approach faces difficulties when modeling the transition region between the surface microstructure and synthetic 3D morphology, leading to surface artifacts (e.g., subsurface 3D grains protruding on the surface) or unrealistic subsurface grains (e.g., concave grains, very small grains needed to close gaps in the transition zone). In Zeghadi et al. (2007), this issue is addressed by expanding or eroding each surface grain along the interior using a systematic process to generate the first layer of the 3D grains, followed by Voronoi seeding for the next layers. Yet, it is worth noting that such a procedure leads to unacceptable grain morphologies just underneath the first layer. As a result, here in this paper, an iterative convexifying process is carried out to improve grain quality. In Lebensohn et al. (2008), the transition zone is rectified by annealing the microstructure using a standard 3D Monte Carlo (MC) grain growth model, where the voxels in the surface layer are fixed and not allowed to evolve while the subsurface grain topology is energetically optimized. However, such an approach requires considerable computational effort. In the presented work, a novel GIVP approach is employed for the 3D reconstruction of polycrystalline microstructures. The approach leads to a single convex hull for each crystal that may overlap with its neighboring grains. The resulting microstructure is subsequently convexified by using a process that eliminates the intersection regions systematically.

The paper is organized as follows: first, within Section 2.1, an overview of Voronoi 2D diagrams is described. Next in Section 2.2, the process of eliminating the overlapping granular regions through a convexification algorithm is explained for a simple 2D micrograph. Afterward, the process of obtaining Voronoi generator points from the micrograph (i.e., GIVP) is discussed in Section 2.3. This is followed by Section 2.4, outlining the algorithm for successively stacking 2D experimental EBSD images and constructing 3D microstructures, while retaining the experimental surface measurements. Subsequently, the implementation of the algorithm for obtaining a convexified 3D microstructure is discussed in Section 2.5. Next in Section 3, an overview of the SEM–DIC experiment, as well as the crystal plasticity finite element method (CPFEM) (Yaghoobi et al., 2019) is provided. Additionally, comparisons are made with surface DIC measurements for random samples of 3D microstructures as compared against the columnar 2D microstructures.

2. Methodology

This section begins with formally defining the Voronoi tessellation and the generator points following the notation used in Suzuki and Iri (1986).

2.1. 2D Voronoi diagram

Let $P(\boldsymbol{x})$ denote a point in the N-dimensional Euclidean space $\mathcal{R}^N$, where $\boldsymbol{x}$ is an N-dimensional vector (i.e., $\boldsymbol{x} = (x^1, x^2, \dots, x^N)$). Given n distinct generator points (e.g., $P_1(\boldsymbol{x}_1)$, $P_2(\boldsymbol{x}_2)$, $\dots$, $P_n(\boldsymbol{x}_n)$) in $\mathcal{R}^N$, the 2D surface can be partitioned to polygons, as follows:

$$Q_i = \bigcap_{j:j\neq i} \{\boldsymbol{x} \in \mathcal{R}^N \mid \|\boldsymbol{x} - \boldsymbol{x}_i\|_2 < \|\boldsymbol{x} - \boldsymbol{x}_j\|_2\} \tag{1}$$

where Q_i denotes a set of points in $\mathcal{R}^N$ that are closer to $P_i(\boldsymbol{x}_i)$ than to any other $P_j(\boldsymbol{x}_j)$ for $i \neq j$. Here, $\|.\|_2$ denotes the Euclidean (i.e., L_2 norm) distance. Hence, each polygon in the diagram contains points that are closer to its center as compared to the center of any other polygon. This partitioning, as shown in Fig. 1(a), is called the Voronoi tessellation for given n generator points (i.e., $P_i(\boldsymbol{x}_i)$ where $i = \{1, 2, \dots, n\}$). The problem of detecting Voronoi polygons is equivalent to finding Voronoi centers, if they exist. If however, the Voronoi centers do not exist (i.e., the polygons are not Voronoi polygons), the points that can best approximate the Voronoi centers are useful to locate (Evans and Jones, 1987).

It is to be noted that two corollaries can follow from Eq. (1): (i) Voronoi polygons are convex in topology, and (ii) the line segment joining centers of adjacent polygons is perpendicularly bisected by the boundary line, common to both polygons.

In a 2D diagram, the generator points can be obtained from the Voronoi tessellation using a purely geometrical method that is based on the property of the Voronoi diagram. In Fig. 1(a), the points P_1, P_2, and P_3 are generators, while V_1 denotes a Voronoi point which is the circumcenter of the triangle $\Delta P_1P_2P_3$. Here, V_2, V_3, and V_4 are the neighboring Voronoi points. Using above denotation, let $\angle V_2V_1V_3 = \alpha$. Consequently, the $\angle P_1P_3P_2$ can be calculated as follows:

$$\angle P_1P_3P_2 = \pi - \alpha \tag{2}$$

Accordingly, from the inscribed angle theorem, the angle formed at the center of the circle by lines originating from two points on the circle's circumference is double the angle formed on the circumference of the circle by lines originating from the same points (i.e., $\angle P_1V_1P_2 = 2(\pi - \alpha)$). Hence, given that the line $\overline{V_1V_4}$ is bisecting the segment $\overline{P_1P_2}$, one can calculate the angles $\angle P_1V_1V_4$ and $\angle P_2V_1V_4$ as follows:

$$\angle P_1V_1V_4 = \angle P_2V_1V_4 = \pi - \alpha \tag{3}$$

Therefore, given an exact Voronoi diagram, a generator can be determined by the intersection of rays such as r_1 and r_2 shown in Fig. 1(b).

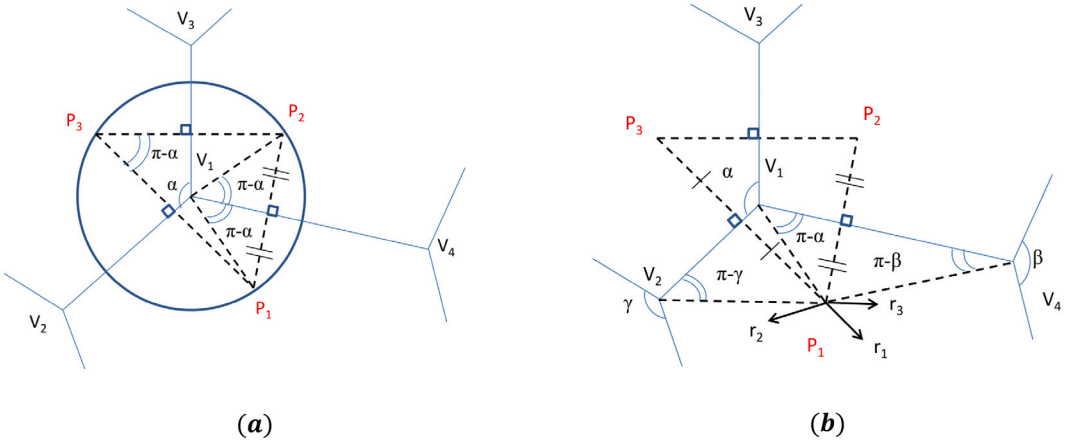

Fig. 1. (a) Voronoi diagram with the generators and Voronoi points, (b) geometrical method to obtain the generator points from the Voronoi diagram.

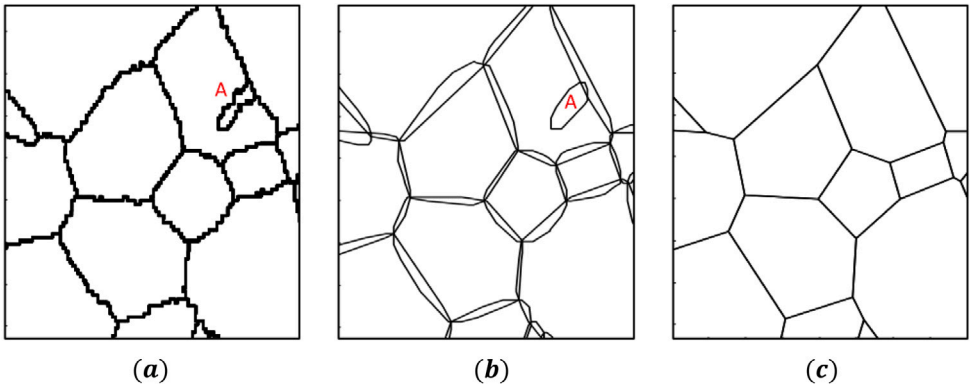

Fig. 2. Method to obtain the 2D convex microstructure: (a) the original experimental microstructure (grain *A* represents a twinned region, which is an internal facet of the parent grain), (b) the convex hulls of individual grains, (c) the resulting convex microstructure after dividing the intersecting regions among the individual grains.

These rays are emanating from the endpoints of a Voronoi edge, V_1 and V_4, respectively. Once the generator point P_1 of a Voronoi region G_1 is obtained, the generators of the regions sharing a common edge with G_1 can also be found. These generators can be interpreted as the mirror images of P_1 with respect to the Voronoi edges bounding G_1. It is proved in Aurenhammer (1987) that a proper convex plane tessellation, all of whose vertices have degree three, is a Voronoi diagram if and only if all rays such as r_1, r_2, and r_3 shown in Fig. 1(b) have a point in common at each region.

2.2. Convex 2D microstructure

During the recrystallization process, the cells grow in space, leading to near-convex microstructures. The microstructures that are used in this study underwent dynamic recrystallization due to a hot rolling process, resulting in fairly equiaxed microstructures. Recrystallized microstructures grow from a nucleus and form an near-convex topology. In this paper, an age-hardened Mg-rare earth alloy WE43-T5, provided in the hot-rolled and aged condition with no intermediate solution treatment, is used. Since the microstructures are almost convex, it would be suitable to construct the equivalent convex microstructure before obtaining the Voronoi generators. It is to be noted that every Voronoi diagram produces convex polygons, but the converse does not always hold true.

Fig. 2 outlines the process of obtaining the 2D convex microstructure from the original micrograph. Fig. 2(a) shows the original microstructure, which is obtained in a rasterized format. The convex hulls of individual grains are constructed from the original microstructure using the *MATLAB* function convhulln, which uses the popular Qhull method. Fig. 2(a)–(b) show an internal facet *A*, which corresponds to a twinned region. It can be observed from Fig. 2(b) that there are many intersecting regions shared by two or three grains that need to be assigned to a unique grain in order to obtain a convex microstructure. The procedure to sort the overlapping region is as follows:

(1) In 2D space, the convex hull is represented by a sequence of boundary points, as indicated in Fig. 3(a). Connecting these boundary points results in the convex polygon. By removing a particular point, the remaining points can still be connected to form convex polygons.

(2) The points of a polygon that are in other polygons are removed, and the intersecting points of the two polygons are included in both cells to form convex grains again. This procedure can be followed for any two intersecting polygons, resulting in the same unique convex microstructure, irrespective of the sequence followed.

Fig. 3 shows the procedure mentioned, applied to grains 1, 2, and 3. Fig. 3(a) shows the grains with their original convex hulls along with their corresponding boundary points. Step 2 is applied to grain 1, resulting in Fig. 3(b). Same procedure is again applied to grain 2, resulting in Fig. 3(c). It is to be seen that after the procedure, every two neighboring grains share an edge with two common points, and every three neighboring grains share a triple point. It can be shown that Step 2 followed in any sequence among the three grains gives the same resulting microstructure. Fig. 2(c) shows the procedure applied to the entire microstructure, resulting in a fully convexified topology. It is to be noted that since the region *A* is an internal facet, it will not be represented in the final microstructure. Additionally, the work in this paper is targeted toward validation of the reconstruction method in a Mg-rare earth alloy at low strains, where experimental evidence indicates low propensity for twinning.

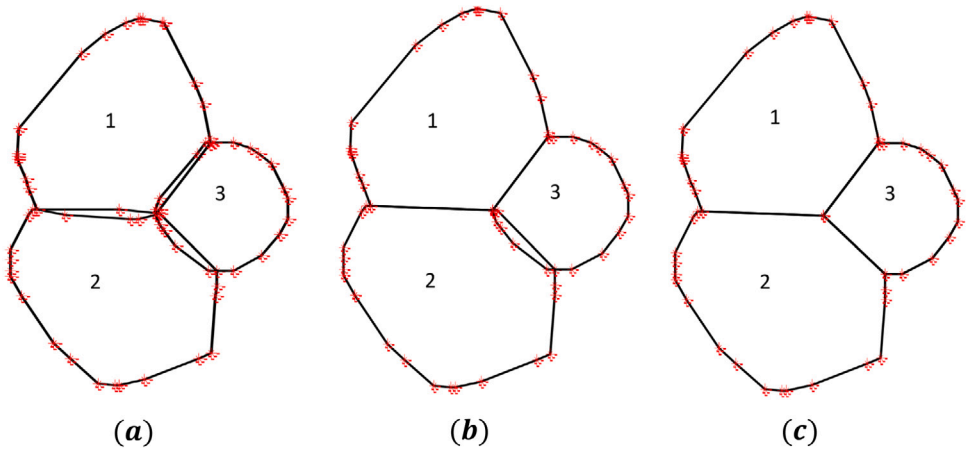

Fig. 3. Method to eliminate the intersecting regions of the convex hulls: (a) grains 1, 2, and 3 with their overlapping convex hulls, (b) Step 2 is followed for grains 1 and 2, (c) Step 2 is followed for grain 3.

2.3. Obtaining Voronoi generators for 2D convex microstructures

Once the convex 2D microstructure is generated, Eq. (3) is used to check whether a unique generator point is achievable for each grain. Fig. 4(a) shows grain A with 6 edges and 6 vertices, respectively surrounded by the neighboring grains B, C, D, E, F, and G. The procedure mentioned earlier in Fig. 1(b) is employed to construct the Voronoi generators A_1, A_2, A_3, A_4, A_5, and A_6 for grain A as well as the corresponding generator points for the neighboring grains. Here, rays r_1, r_2, r_3, r_4, r_5, and r_6 are constructed by connecting the generator points A_1, A_2, A_3, A_4, A_5, and A_6 to their respective vertices. It can be seen from Fig. 4(a) that the rays do not converge to a single point as in case for a Voronoi diagram.

Since the aim is to represent the convex microstructure with Voronoi generators, multiple generators are used to represent each grain as opposed to a single generator point. Here, each grain is represented by as many Voronoi generators as the number of vertices of the grain. Fig. 4(b) illustrates the Voronoi polygons corresponding to each grain using dashed lines. For regular-shaped convex grains, the microstructure can be represented by placing Voronoi generators along the vertices or triple-points of the microstructure. In this paper, the same radius of circumcircle r is used for obtaining generator points at all the vertices of the grain.

The method is also anomaly applicable for long slender grains, as shown in Fig. 5. Fig. 5(a) depicts the inverse Voronoi representation of grains A, B, and C. It can be seen that the Voronoi regions of grain A corresponding to the vertices P and Q cut into grain B, as indicated by the red box. Similarly, the Voronoi region of grain B corresponding to vertex R cuts into grain C. This is due to the fact that the grains A and B are slender with edges $\overline{RS}$ and $\overline{TU}$ much longer than $\overline{PR}$, $\overline{QS}$, and $\overline{RT}$. The issue can be addressed by using additional generator points at the midpoint of the edges $\overline{RS}$ and $\overline{TU}$, as shown in Fig. 5(b). In this case, the Voronoi regions of the generator points are bounded within the convex envelope of grains A and B.

Hence, the non-convex or slender microstructures with high-aspect ratio (e.g., lathe-like morphologies) can be addressed by composing such structures using several generator points within the grain. Such an approach will be addressed in future work.

In this paper, additional generator points are not added to the slender grains, since the convex surface microstructure is regenerated by convexifying the 3D microstructure, as explained in Section 2.5. Hence, as the generator points are identified for the 2D micrograph, a 3D microstructure can now be created by stacking the Voronoi generator points beneath the surface image. This is followed by a convexification process that ensures the measured surface image is properly retained throughout the reconstruction. This process is described next.

2.4. Construction of 3D microstructure using Voronoi generators

Once the Voronoi generators are identified for the 2D micrograph, a 3D microstructure can be readily created by adding Voronoi generator points in the z-direction. Here, a large surface observation such as an EBSD map is used to find the generators and their representative orientations. As a result, multiple sections of the EBSD map are randomly selected and stacked up beneath the measured surface image, as illustrated in Fig. 6, in the z-direction. The following assumptions are made while generating the 3D microstructure:

(1) The grains are equiaxed. With no information about the grain shape in the z-direction, it would be useful to assume equiaxed morphology for each grain. Therefore, the grains in layers with a gap-width of grain size d, as it is apparent from the 2D observation, are stacked above one another. Here, the microstructural images are stacked by a spacing of size d to mimic an equiaxial microstructure in the z-direction. Decreasing or increasing the value would increase anisotropy in the z-direction.

(2) The surface EBSD map is representative of the microstructure in the x–y plane across the depth of the sample. That is, the surface orientation distributions are representative of the bulk orientation distributions, which is true in the case of rolled textures where ND direction represents the z-direction as well as random textures arising out of solidification processes.

(3) The grains in the sections of the EBSD map are represented by their centroid as Voronoi generators. It is assumed that the overall texture of the 3D microstructure does not change considerably by this assumption. Alternatively, one could convexify the sections and represent them by Voronoi points as discussed in Sections 2.2 and 2.3.

To represent the distribution of Voronoi points in the z-direction, the generator points along each section are perturbed within the z-direction by a normal distribution with a standard deviation equivalent to the mean grain diameter (i.e., $\sigma = d/2$). The scanned microstructure of interest in this paper comprises of grains with average grain size of $d = 13$ μm with a standard deviation of about 6.5 μm. Alternatively, for a more general case where the distribution of grain diameters is unknown, the Voronoi generators can be perturbed by $\pm d/2$ along the z-direction using a uniform random distribution. Additionally, to account for the tilt and twist of the grain boundaries, the Voronoi generators of the topmost layer are perturbed in the z-direction by a normal distribution with a standard deviation that is equal to the radius of the circumcircle (i.e., $\sigma = r$). Here, the standard deviation is chosen such that the generator points still lie close to the surface of the microstructure, while providing tilt and twist of the grain boundaries. The Voronoi diagram is recreated in 3D with the resultant Voronoi points. Fig. 6 illustrates a schematic representation of the construction, resulting in a representative 3D microstructure.

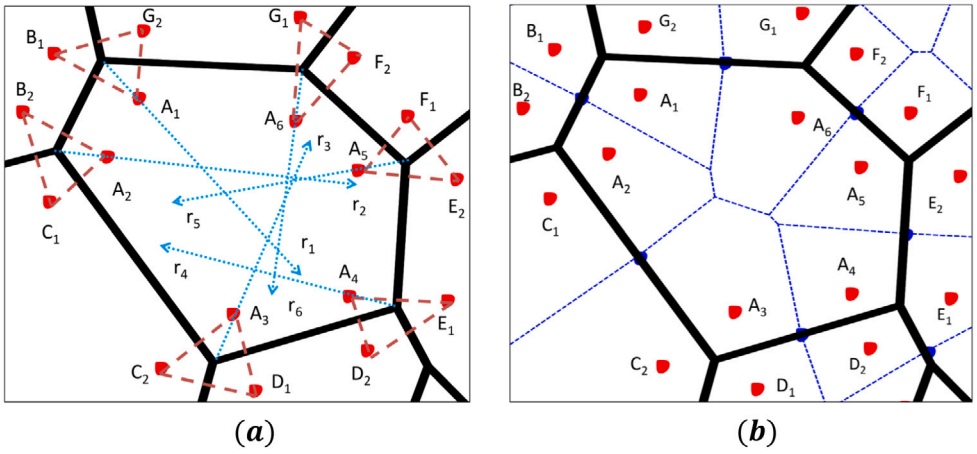

Fig. 4. Method to obtain the generator points from a convex microstructure: (a) rays r_1, r_2, ..., r_6 do not converge to a single point, therefore the grain A is represented by six Voronoi generators A_1, A_2, ..., A_6, (b) the Voronoi regions of the grain is indicated by dashed lines.

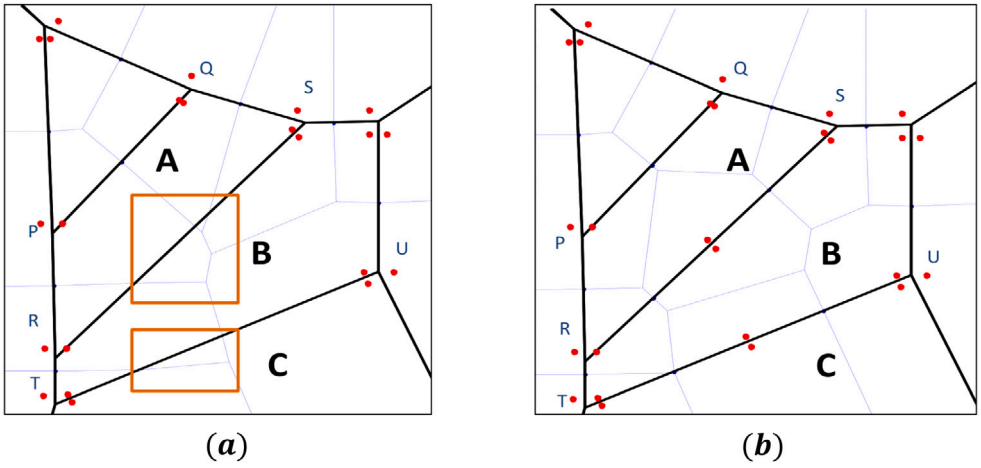

Fig. 5. In the case of slender grains, Voronoi regions corresponding to some of the generator points can extrude into the neighboring grains across the long edges. (a) Voronoi regions of slender grains A and B extrude into grains B and C as indicated by the boxed regions. (b) Additional generator points are placed along the midpoint of edges $\overline{RS}$ and $\overline{TU}$ to bound the Voronoi regions within the grain.

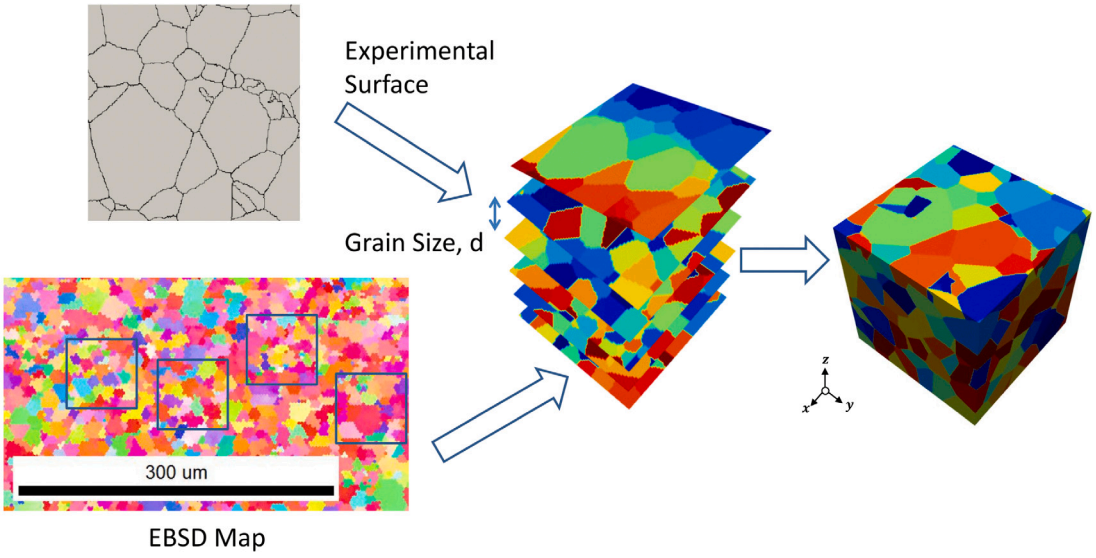

Fig. 6. Schematic diagram showing the construction of 3D microstructure from the given surface observation and EBSD map. Sections of the EBSD map are randomly chosen and stacked below the microstructure using their centroid as Voronoi generators.

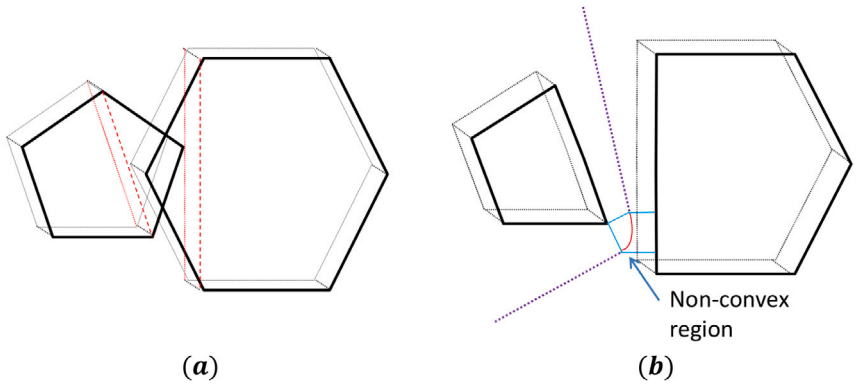

Fig. 7. Method to convexify the 3D microstructure: (a) the intersecting points of the convex hulls of the grains are removed; (b) the voxels within the gap between the grains are reassigned to its nearest grain using a linear least-square solver, the non-convex region of the partition is indicated.

2.5. Convexification of 3D microstructure

It can be observed from Fig. 6(rightmost) that the grains in the top layer are penetrated by the Voronoi generator points beneath the surface. Hence, a convexification approach is implemented to recover the original surface microstructure. The property of convex hulls is employed, such that every section of a 3D convex polygon results in a 2D convex shape. Since 2D convex diagrams are obtained with the surface image, the surface microstructure can be fully recovered by convexifying the entire 3D microstructure. The problem of slender grains mentioned in Section 2.3 is also solved by convexifying the entire 3D microstructure. The procedure for convexification of the 3D microstructure is similar to the process of convexification, followed in Section 2.2. The modified 3D approach is described below for creation of the 3D solid microstructure:

(1) The convex hulls of individual grains are recreated using the *MATLAB* function convhulln.

(2) The points of a polygon that are penetrated in other polygons are eliminated, as shown in Fig. 7(a). Instead of finding the intersecting planes of the convex hulls, the convex hulls of the grains are reconstructed using the remaining vertices, as illustrated in Fig. 7(b).

(3) The gaps between the crystals are assigned to the nearest grain using a linear least-squares solver. The problem of finding the smallest distance of a given voxel to the grain can be described as:

$$\min_{x} \frac{1}{2}\|x - v\|_2^2 \qquad \boldsymbol{A}x \leq b \tag{4}$$

where v corresponds to the voxel to be assigned, and $\boldsymbol{A}x = b$ represents the planes enclosing each grain. Here, the voxel v is assigned to the nearest grain in the Euclidean norm sense. Fig. 7(b) shows the partition between the grains by assigning each of the overlapping voxels to the nearest grain as described. The regions near the edges of the grain are assigned in a non-planar way, as indicated in Fig. 7(b). Such a process results in some non-convex regions in the 3D-microstructure. Exact 3D convex microstructures can be obtained by following the procedure in Section 2.2.

Fig. 8 illustrates the initial 3D microstructure and the resulting convexified structure. Fig. 9 shows the top three layers of the 3D microstructure before and after the convexification process. It can be observed that convexification affects only the top two layers, whereas the layers underneath remain convexified due to the nature of the Voronoi diagram.

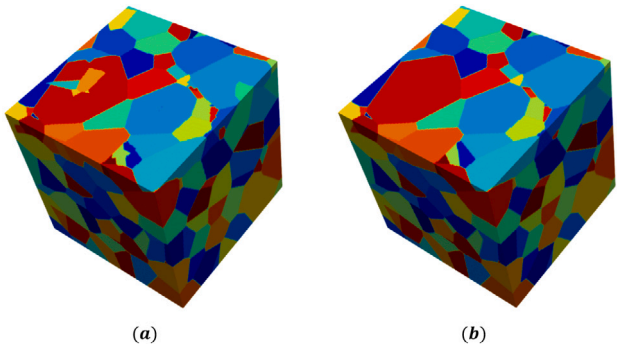

Fig. 8. Convexification of 3D microstructure: (a) original microstructure generated by stacking up the Voronoi generators, (b) the convexified 3D microstructure.

3. Results and discussion

The above algorithms are implemented on an experimental microstructure obtained from SEM–DIC technique for WE43-T5 alloy. The surface strains are measured using SEM by tracking nanoparticles embedded in the alloy. The details of the experimental procedure are described in Githens et al. (2020), Ganesan et al. (2021). The measured microstructure is of dimensions 75 μm × 75 μm and is previously shown in Fig. 6. The microstructure comprises of 49 grains initially. However, after the process of 2D convexification as described in Section 2.2, the number of grains shrinks to 46, as the twinned regions such as one shown in Fig. 2(a) are removed during the 2D convexification process.

The surface EBSD map, as obtained from experiments, is of dimensions 600 μm × 700 μm and comprises of 6000 grains. The average grain size of the 2D EBSD map is found to be $d = 13$ μm with a standard deviation of about 6.5 μm. The procedure mentioned in Section 2.4 is followed by selecting five random windows from the surface EBSD image with dimensions 75 μm × 75 μm, with some windows identified in Fig. 6. These collections of grains are subsequently stacked below the original experimental microstructure using a spacing of grain size d and perturbed in the z-direction by a normal distribution with a standard deviation of $\sigma = d/2 = 6.5$ μm. The resulting microstructure is then convexified to obtain the 3D microstructural realizations as shown in Fig. 10(b)–(c). These are referred to as the variants 1 and 2 of the 3D microstructure. The variant 1 comprises of 340 grains, whereas the variant 2 comprises of 367 grains. The constructions of these two variants are made by using different windows from the EBSD map followed by a unique random perturbation of the generator points along z-direction. Here, the reconstruction simulations are performed on a single 2.6 GHz Intel Core i5 processor machine. The total computational time for generation of Variants 1 and 2 with a 100 × 100 × 100 voxel resolution was in the order of 5000–7000 s (i.e. about 2 h). A lower 50 × 50 × 50 resolution can significantly decrease the total computational cost to the order of 1100–1400 s (i.e., about 20 min). Furthermore, a parallel processing implementation of such an algorithm can reduce the run-time and help to solve larger reconstruction problems, such an implementation is to be considered for future studies.

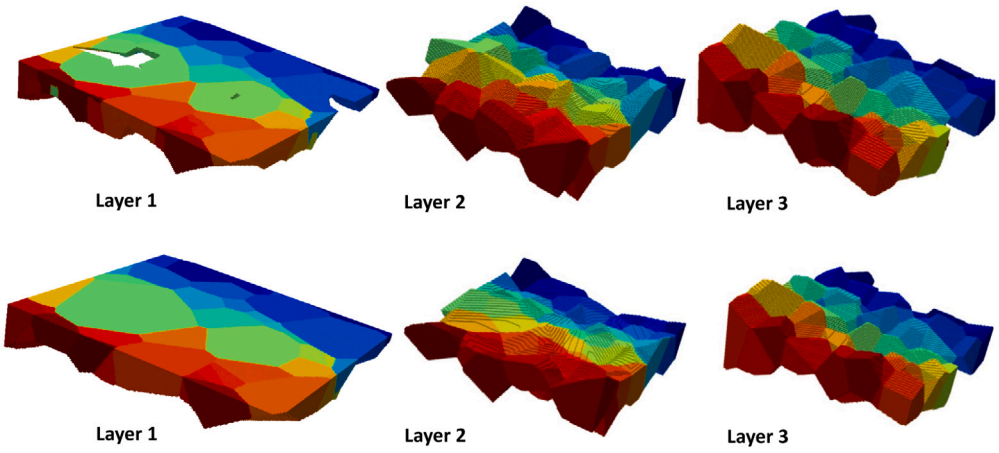

Fig. 9. The First three layers of the 3D microstructure before convexification are shown on the top. The same three layers of the microstructure after convexification procedure are depicted below. Here, each color represents a different grain ID.

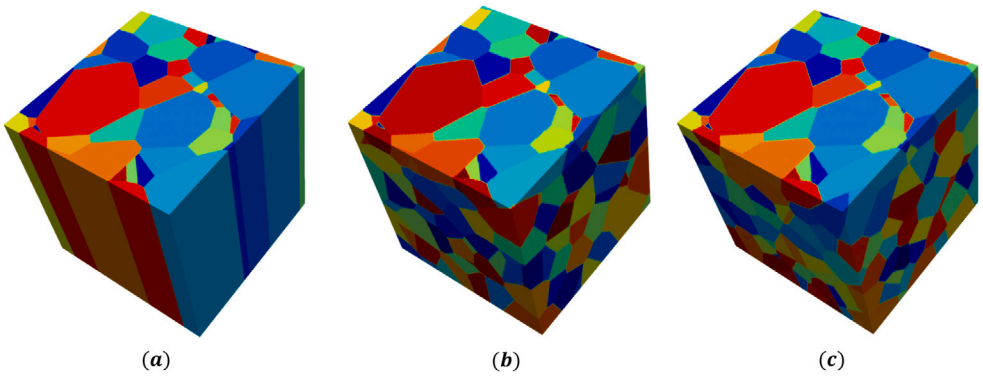

Fig. 10. Three microstructures considered in this paper are (a) convexified columnar microstructure with 46 grains, (b) variant 1 with 340 grains, and (c) variant 2 with 367 grains. Here, different stacks of EBSD images are used to build the variants 1 and 2. Additionally, for each microstructure, the perturbation of generator points along z-direction are distinct due to it being assigned randomly.

Additionally, two more examples were generated to demonstrate the methodology of obtaining convexified 3D microstructures. They are added as a supplementary material in Appendix A.

The pole figures corresponding to (0001), $(10\bar{1}0)$, and $(10\bar{1}1)$ for the resultant 3D microstructures are plotted in Fig. 11. It can be inferred from the plots that the texture of the variants 1 and 2 is on par with the texture from experiment. This is naturally the case with the reconstruction procedure since it samples sections from the surface EBSD scans to generate the 3D microstructure. The sampling determines the uncertainty range in pole figures (Acar and Sundararaghavan, 2017) as seen in the 3D reconstructions.

Using these microstructures, a 3D CPFE PRISMS-Plasticity code (Yaghoobi et al., 2019) based on a fully implicit implementation of an elastoplastic single crystal model is used to capture strains under loading. Here, 8 noded linear brick elements are used to discretize the volume. The CPFE simulations use between 60 and 200 cores depending on available resources in the shared cluster. Computational details including solve and assembly time for the PRISMS-Plasticity code can be found in Yaghoobi et al. (2019). Within the simulations, the x and y displacements from experiments are applied along all the lateral surfaces (similar to the measured experimental data on the surface). Furthermore, the top and bottom surfaces are traction-free with z displacement constrained at the origin. Crystallographic slip, twinning, and reorientation of crystals are assumed to be the primary mechanisms of plastic deformation. For a material with $\alpha = 1, \ldots, N$ slip/twin systems; the resistances $s^{\alpha}(t) > 0$ offered by the slip/twin systems at time t depends on the plastic shearing rates $\dot{\gamma}^{\alpha}$ on systems α through a hardening law:

$$\dot{s}^{\alpha}(t) = \sum_{\beta=1}^{N} h^{\alpha\beta} \|\dot{\gamma}^{\beta}\| \tag{5}$$

where,

$$s^{\alpha}(t=0) = s_o^{\alpha}$$
$$h^{\alpha\beta} = h_o^{\beta}(q + (1-q)\delta^{\alpha\beta})(1 - \frac{s^{\beta}}{s_{sat}^{\beta}}) \tag{6}$$

where the slip system hardening term, denoted as $h^{\alpha\beta}$, includes latent hardening through parameter q, taken to be 1 for coplanar slip systems and 1.4 for non-coplanar slip systems (Anand and Kothari, 1996). The parameter s_o^{α} is the initial critical resolved shear stress for system α, and h_o^{β} and s_{sat}^{β} are the hardening rate and saturation resistance of slip system β, respectively. These three parameters are calibrated for each slip system such that the CPFE model predicts the experimental stress–strain response under different deformation modes. Other aspects of the model, including elastoplastic decomposition, flow rule, and constitutive update algorithm, are detailed in Yaghoobi et al. (2019).

The volume fraction associated with each twinning system, denoted as g^{n,t_i}, increases with loading, and the fraction at quadrature point n at any given loading step is given by:

$$g^{n,t_i} = \sum_{steps} \Delta g^{n,t_i} \tag{7}$$

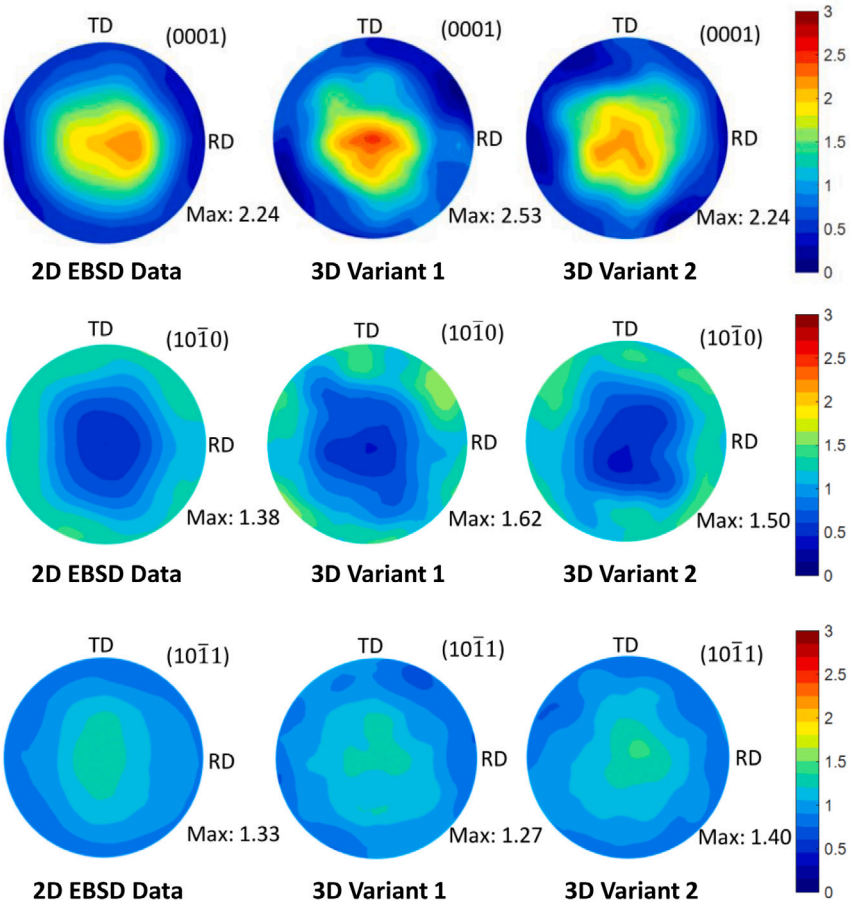

Fig. 11. The recalculated pole figures for 2D EBSD data as well as 3D variants 1 and 2 in (0001), (10$\bar{1}$0), and (10$\bar{1}$1) directions are shown, respectively.

Table 1
Hardening parameters for simulating stress–strain curves.

Mode	s_o^a (MPa)	h_o (MPa)	s_{sat} (MPa)
Basal$_{\langle a\rangle}$	76.0	225.6	248.7
Prism$_{\langle a\rangle}$	163.2	124.9	356.3
Pyram$_{\langle a\rangle}$	160.3	120.2	347.8
Pyram$_{\langle c+a\rangle}$	187.4	237.9	350.4
Twin$_{\langle c+a\rangle}$	116.4	105.6	238.3

where,

$$\Delta g^{n,t_i} = \frac{\Delta\gamma^{n,t_i}}{S} \tag{8}$$

where t_i denotes the twinning system i, S is the characteristic shear strain of the twin, and $\Delta\gamma^{n,t_i}$ is the shear increment of the twin system at the loading step. For pure magnesium and Mg-alloys, $S = 0.129$. The total fraction of twins is calculated locally at each quadrature point. If it exceeds a critical value (i.e., $\sum_i g^{n,t_i} > F_T$), the quadrature point is reoriented. Here, F_T is taken to be 0.25 based on the predominant twin reorientation (PTR) scheme in Solomon and Marquis (2018). The crystal elastic parameters for Mg alloy are taken to be: $C_{11} = 59.3$, $C_{12} = 25.7$, $C_{13} = 21.4$, $C_{33} = 61.5$, and $C_{55} = 16.4$ (in GPa) (Kammers and Daly, 2013). The calibrated hardening parameters employed for the basal, prismatic, pyramidal, and twin systems are tabulated in Table 1.

The stress–strain curves of the variants 1 and 2 of 3D microstructures are generated for both pure tension and compression boundary conditions with a mesh of 100 × 100 × 100 elements using PRISMS-Plasticity code (Yaghoobi et al., 2019). The results of the stress–strain relationship are plotted in Fig. 12 and compared against the experimental stress–strain curves. The results show an excellent match between the experiments and the simulations.

The objective of the next exercise is to compare the CPFE surface strain results against DIC data for the reconstructed microstructures (e.g., variants 1 and 2) as well as a simple columnar representation, as seen in Fig. 10(a), of the surface grains. The approach is used to ascertain the sensitivity of the surface measurements to the underlying microstructure. Since the 3D boundary conditions are unknown from surface measurements, the measured surface displacements are primarily extended on the outer surface along the z-axis. As shown in the inset underneath the legend in Fig. 13, the test corresponds to tension along with the x-axis of the microstructure.

The map of the principal strain from experiments, denoted as ϵ_1, is given in Fig. 13(a). Individual grains A–H are marked in order to investigate the variation in strains between columnar and the variants of the 3D microstructures. The corresponding map from our simulations on columnar and 3D variants 1 and 2 are indicated in Fig. 13(b)–(d), respectively. It can be seen that the surface strain maps are similar across all observed morphologies and compare well with the experiments.

Note that the experimental data also contains slip traces that indicate the activity of different slip systems within the grains. These slip bands cannot be directly captured in CPFE and need to be inferred from the computed shearing rates, $\dot{\gamma}^\alpha$, for different slip and twinning systems. To better compare the surface observations, the relative activity of the individual slip systems (basal, prismatic, pyramidal$_{\langle a\rangle}$, pyramidal$_{\langle c+a\rangle}$, and twinning) are calculated and shown in Fig. 14. The measured slip traces from experiments are shown on the left. The grains in the experimental results are colored according to the Schmid factor for the basal slip system. In grains with high basal Schmid factor, the basal slip is typically active, and this trend is seen from all three cases considered. For grains with low basal Schmid factor, the activated non-basal slip modes show variations across the three cases.

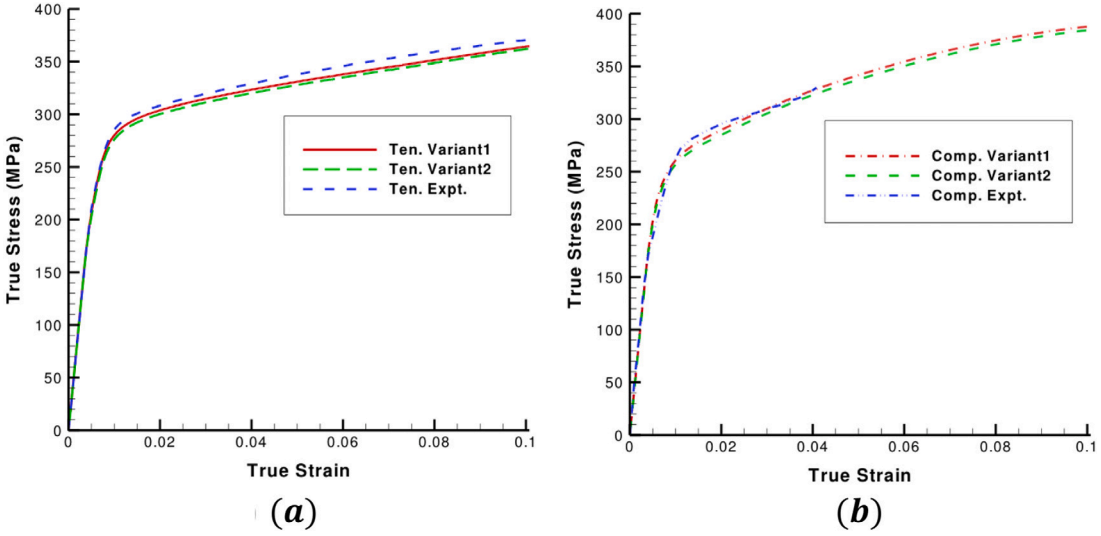

Fig. 12. Experimental and simulated stress–strain curves for (a) tension (b) compression.

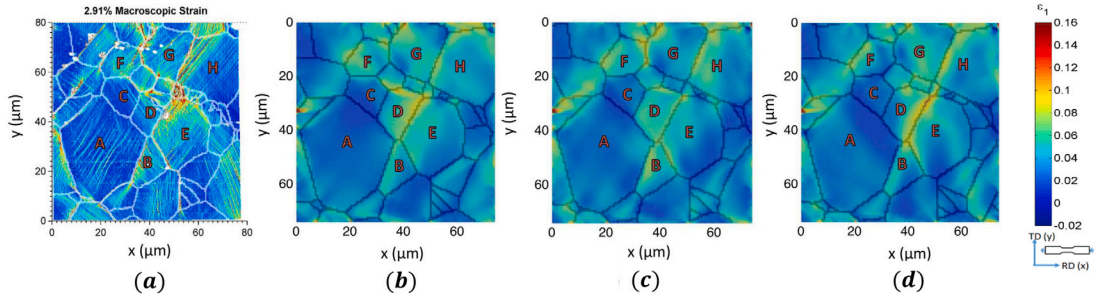

Fig. 13. Comparison of principal strain ϵ_1 from (a) SEM–DIC experiment, (b) convexified columnar microstructure, (c) 3D variant 1, and (d) 3D variant 2 are illustrated.

From Fig. 14, it can be seen that grain A depicts predominantly prismatic activity in columnar microstructure and variant 1, whereas it shows both prismatic and pyramidal$_{\langle a \rangle}$ activity in variant 2 of the microstructure. Additionally, grain B exhibits twinning activity in all three variants. Grain C observes pyramidal$_{\langle c+a \rangle}$ activity for both columnar microstructure and variant 1, whereas it shows predominantly prismatic slip activity in variant 2 as is also seen in the experiment. Grain D also exhibits both basal and twin activities within all three microstructures. Grain E predominately shows basal slip activity in all three microstructures, as also in the experiment. However, pyramidal$_{\langle a \rangle}$ activity of variant 2 can also be distinctly observed in grain E. Grains F and G exhibit basal and pyramidal$_{\langle a \rangle}$ slip activity for all three microstructures, in line with the experiment. Grain H shows basal slip activity for the columnar variant, whereas it shows both basal and twin activity for 3D variants 1 and 2. It can be seen that the slip activity in grains A, C, E, and H of microstructure variant 2 varies from the columnar microstructure. Grains A, C, and E also show differences in slip activity between 3D variant 1 and 3D variant 2. These grains were chosen to study the effect of the underlying microstructure. The slip activity at different depths of the material for the 3D variant 2 is particularly studied.

The relative slip activity of the variant 2 microstructure at various depths are plotted in Fig. 15. Variations in non-basal activity occur due to 3D grain structure when strong basal slip activation in underlying grains triggers other non-basal systems in surface grains with low basal Schmid factor. It can be observed in case of grain A where both prismatic and pyramidal$_{\langle a \rangle}$ activities are observed, the region of pyramidal$_{\langle a \rangle}$ activity is due to the grains underneath the surface, such as M and L. These two grains, as shown in Fig. 15, exhibit strong basal slip activity. Other factors such, as slip systems that allow favorable transmission of loads across misoriented subsurface grains, are also at play. The region of grain E, which observes pyramidal$_{\langle a \rangle}$ activity arises possibly from the grain J, which also exhibits pyramidal$_{\langle a \rangle}$ activity. It is also observed that grains D and G extend far deeper into the surface of 3D microstructure, and hence show little differences in observed slip modes as compared to columnar microstructures. As a summary, these results indicate the influence of subsurface grains in determining slip modes on surface grains and the need for statistical analysis based on 3D realizations for comparing slip activity observed from DIC and CPFEM calculations.

In the case of non-convex microstructures, the reconstruction algorithm in its current format would convexify every non-convex grain in the microstructure through the process described in Section 2.2 and eliminate all the internal granular facets. Nevertheless, realistic microstructures are generally non-convex in topology, especially for the case of 3D microstructures developed by non-equilibrium processes such as 3D printing. Here, several experimental EBSD images are required to capture the average grain size in the z-direction. This can help in determining the length between stacked slices for 3D reconstruction, as discussed in Section 2.4. Alternatively, the additional imaging could be used to build the microstructure by stacking EBSD slices in x or y direction as opposed to the z-direction. Hence, a future extension of the current algorithm based on multiple generator points can be used to model non-convex microstructures. This can be done by first partitioning the non-convex granular domain into a sum of convex subgrains using an already available algorithm such as triangulation, Hertel–Mehlhorn algorithm, and Chazelle's complex cubic algorithm. Using such methods, the twinned region can be better represented as separate internal facets within the grains, and the remaining grain can be split into multiple convex domains. Such an approach is out of the scope of the current paper and will be directed in future.

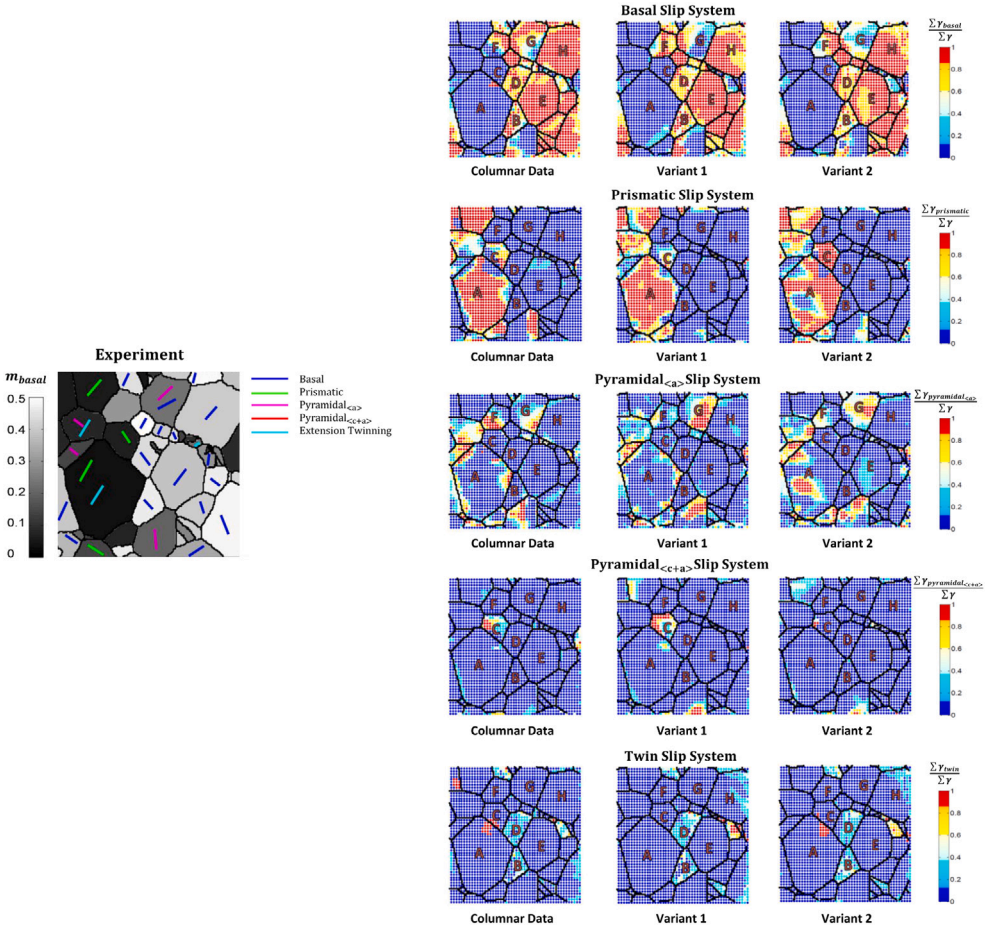

Fig. 14. Comparison of relative activity of the various slip systems using quadrature point data from CPFE model for columnar microstructure, 3D variants 1 and 2. The m_{basal} denotes the Schmid factor for the basal slip system. (For interpretation of the references to color in this figure legend, the reader is referred to the web version of this article.)

4. Conclusions

In this paper, an approach for the construction of 3D microstructures from 2D surface images through Voronoi tessellation is developed. The key novelty from classical reconstruction methods is that the surface microstructure is retained. The issue of realism of the transition region between the surface and subsurface microstructure is addressed using an efficient generalized inverse Voronoi approach with a convexification step. Crystal plasticity numerical models are used for comparing the predicted surface strains in the reconstructed 3D microstructures against experimental measurements. It is observed that the surface strains of different 3D reconstructed microstructures are qualitatively similar to the experiment. However, strong basal slip activation in some subsurface grains may influence the choice of activated slip systems on surface microstructure. Thus, the results presented in this work show the implications of performing a full 3D analysis of measured surface data as compared to only analyzing a 2D extruded model.

Declaration of competing interest

The authors declare that they have no known competing financial interests or personal relationships that could have appeared to influence the work reported in this paper.

Acknowledgments

The authors would like to acknowledge the Air Force Office of Scientific Research Materials for Extreme Environments Program (Grant No. FA9550-18-1-0091) as well as the National Science Foundation Graduate Research Fellowship Program (Grant No. DGE 1256260) for financial support. Gratitude is expressed to Samantha Daly (from the Mechanical Engineering Department at University of California Santa Barbara) for providing SEM–DIC data. Additionally, the computations have been carried out as part of research supported by the U.S. Department of Energy, Office of Basic Energy Sciences, Division of Materials Sciences and Engineering (Grant No. DE-SC0008637) that funds the PRedictive Integrated Structural Materials Science (PRISMS) Center at the University of Michigan.

Appendix. Supplementary microstructural data

Similar to the microstructural examples illustrated in Figs. 6–10, two additional examples, denoted as M_1 and M_2, are generated here to further demonstrate the methodology described in Section 2 of the paper. For both additional examples M_1 and M_2, the measured microstructures on top are of dimensions 75 μm × 75 μm as shown in Fig. S1(a) and Fig. S2(a), respectively. These 2D microstructures respectively consist of 71 and 42 grains, as apparent from the experimental SEM images. However, after the process of 2D convexification as described in Section 2.2, the number of grains shrinks to 65 and 37, as illustrated in Fig. S1(b) and Fig. S2(b), respectively, since the twinned regions such as one shown in Fig. 2(a) are removed via the 2D convexification process in Section 2.2.

Here, the same surface EBSD map, as obtained from experiments, which is of dimensions 600 μm × 700 μm and comprises of 6000 grains is used to generate the corresponding layers of the 3D microstructures with dimensions 75 μm×75 μm, while successively stacking them below

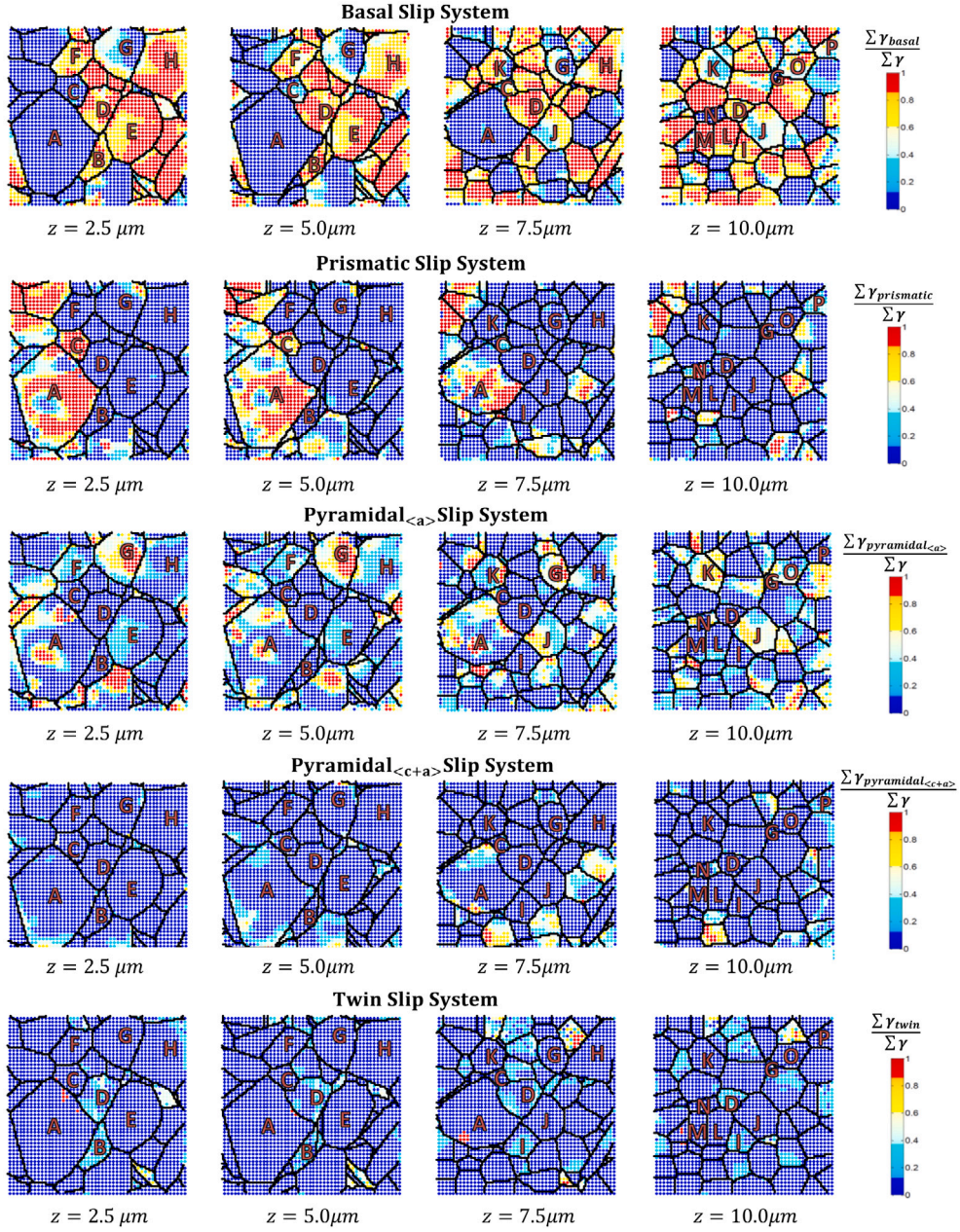

Fig. 15. Comparison of the relative activity of the various slip systems using quadrature point data from CPFE model for 3D variant 2 along the depth of the sample. (For interpretation of the references to color in this figure legend, the reader is referred to the web version of this article.)

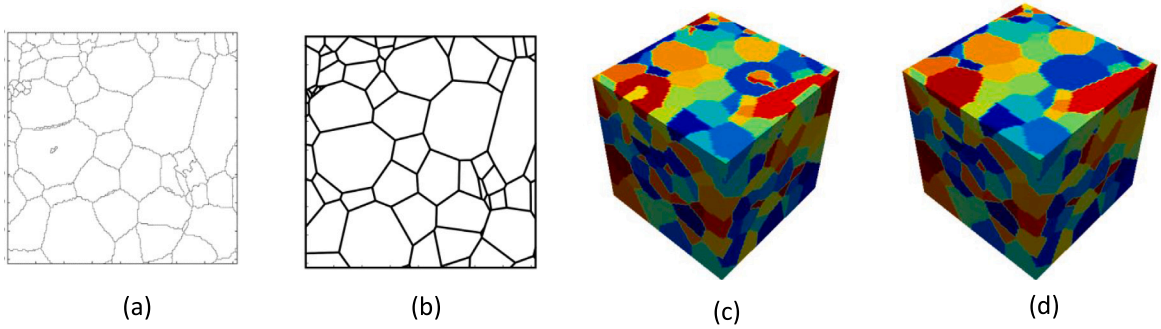

Fig. S1. Additional example, M_1, for demonstrating the reconstruction methodology to obtain a 3D convexified microstructure: (a) original experimental surface microstructure, (b) 2D convexified microstructure, (c) 3D microstructure generated by stacking up the Voronoi generators, and (d) convexified 3D microstructure.

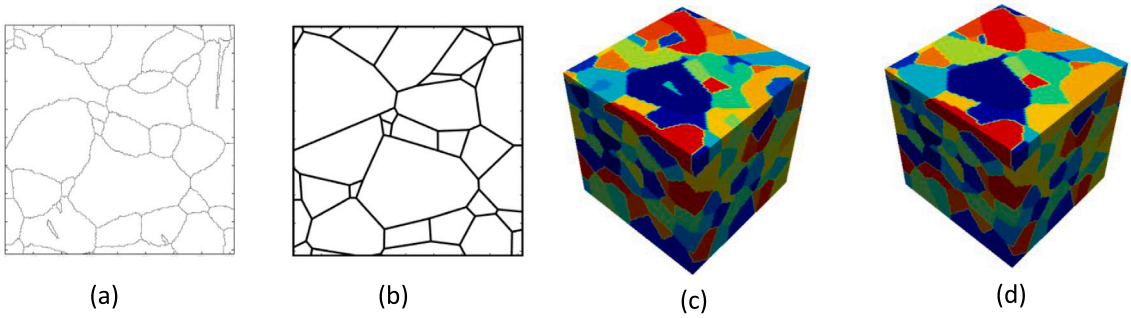

Fig. S2. Additional example, M_2, for demonstrating the reconstruction methodology to obtain a 3D convexified microstructure: (a) original experimental surface microstructure, (b) 2D convexified microstructure, (c) 3D microstructure generated by stacking up the Voronoi generators, (d) convexified 3D microstructure.

the experimental microstructure using a spacing of grain size d. This is followed by perturbing the Voronoi generator points in the z-direction using a normal distribution with a standard deviation of $\sigma = d/2$. The resulting microstructures are then convexified to obtain the 3D microstructural realizations, M_1 and M_2, as depicted in Fig. S1(d) and Fig. S2(d). Here, the additional example M_1 comprises of 421 grains, whereas the example M_2 consists of 395 grains. In addition to having different microstructure surfaces at the top, the stacking layers in examples M_1 and M_2 vary as they are randomly selected from the EBSD map seen in Fig. 6. Also, the perturbation of the generator points along z-direction would be different for both microstructures due to them being assigned via a Gaussian distribution.

References

Acar, Pinar, Sundararaghavan, Veera, 2017. Uncertainty quantification of microstructural properties due to variability in measured pole figures. Acta Mater. 124, 100–108.

Anand, L., Kothari, M., 1996. A computational procedure for rate-independent crystal plasticity. J. Mech. Phys. Solids 44 (4), 525–558.

Aurenhammer, Franz, 1987. Recognising polytopical cell complexes and constructing projection polyhedra. J. Symbolic Comput. 3 (3), 249–255.

Banerjee, Sandip, Bhattacharya, Bhargab B, Das, Sandip, Karmakar, Arindam, Maheshwari, Anil, Roy, Sasanka, 2013. On the construction of generalized voronoi inverse of a rectangular tessellation. In: Transactions on Computational Science XX. Springer, pp. 22–38.

Bargmann, Swantje, Klusemann, Benjamin, Markmann, Jürgen, Schnabel, Jan Eike, Schneider, Konrad, Soyarslan, Celal, Wilmers, Jana, 2018. Generation of 3D representative volume elements for heterogeneous materials: A review. Prog. Mater. Sci. 96, 322–384.

Bhattacharyya, Abhishek, El-Danaf, Ehab, Kalidindi, Surya R, Doherty, Roger D, 2001. Evolution of grain-scale microstructure during large strain simple compression of polycrystalline aluminum with quasi-columnar grains: OIM measurements and numerical simulations. Int. J. Plast. 17 (6), 861–883.

Bostanabad, R., Chen, Wei, Apley, D.W., 2016. Characterization and reconstruction of 3D stochastic microstructures via supervised learning. J. Microsc. 264 (3), 282–297.

Brahme, A., Alvi, M.H., Saylor, D., Fridy, J., Rollett, A.D., 2006. 3D reconstruction of microstructure in a commercial purity aluminum. Scr. Mater. 55 (1), 75–80.

Escoda, Julie, Jeulin, Dominique, Willot, François, Toulemonde, Charles, 2015. Three-dimensional morphological modelling of concrete using multiscale Poisson polyhedra. J. Microsc. 258 (1), 31–48.

Evans, David G., Jones, Steven M., 1987. Detecting Voronoi (area-of-influence) polygons. Math. Geol. 19 (6), 523–537.

Ganesan, Sriram, Yaghoobi, Mohammadreza, Githens, Alan, Chen, Zhe, Daly, Samantha, Allison, John E, Sundararaghavan, Veera, 2021. The effects of heat treatment on the response of WE43 Mg alloy: crystal plasticity finite element simulation and SEM-DIC experiment. Int. J. Plast. 137, 102917.

Githens, A, Ganesan, S, Chen, Z, Allison, J, Sundararaghavan, V, Daly, S, 2020. Characterizing microscale deformation mechanisms and macroscopic tensile properties of a high strength magnesium rare-earth alloy: A combined experimental and crystal plasticity approach. Acta Mater. 186, 77–94.

Groeber, Michael A., Jackson, Michael A., 2014. Dream. 3D: a digital representation environment for the analysis of microstructure in 3D. Integr. Mater. Manufact. Innov. 3 (1), 56–72.

Heilbronner, Renée, Keulen, Nynke, 2006. Grain size and grain shape analysis of fault rocks. Tectonophysics 427 (1-4), 199–216.

Javaheri, Iman, Sundararaghavan, Veera, 2020. Polycrystalline microstructure reconstruction using Markov random fields and histogram matching. Comput. Aided Des. 120, 102806.

Jiao, Yang, Chawla, Nikhilesh, 2014. Three dimensional modeling of complex heterogeneous materials via statistical microstructural descriptors. Integr. Mater. Manufact. Innov. 3 (1), 25–43.

Kammers, Adam D., Daly, Samantha, 2013. Digital image correlation under scanning electron microscopy: methodology and validation. Exp. Mech. 53 (9), 1743–1761.

Lebensohn, Ricardo A, Brenner, Renald, Castelnau, Olivier, Rollett, Anthony D, 2008. Orientation image-based micromechanical modelling of subgrain texture evolution in polycrystalline copper. Acta Mater. 56 (15), 3914–3926.

Nicolas, Andrea, Mello, Alberto W, Sun, Yiwei, Johnson, David R, Sangid, Michael D, 2019. Reconstruction methods and analysis of subsurface uncertainty for anisotropic microstructures. Mater. Sci. Eng. A 760, 76–87.

Okabe, Atsuyuki, 1992. Spatial Tessellations. Wiley Online Library.

Panozzo, R., Hurlimann, H., 1983. A simple method for the quantitative discrimination of convex and convex-concave lines. Microsc. Acta 87 (2), 169–176.

Quey, Romain, Dawson, P.R., Barbe, Fabrice, 2011. Large-scale 3D random polycrystals for the finite element method: Generation, meshing and remeshing. Comput. Methods Appl. Mech. Engrg. 200 (17), 1729–1745.

Schoenberg, Frederic Paik, Ferguson, Thomas, Li, Cheng, 2003. Inverting dirichlet tessellations. Comput. J. 46 (1), 76–83.

Solomon, Ellen L.S., Marquis, Emmanuelle A., 2018. Deformation behavior of β and β precipitates in Mg-RE alloys. Mater. Lett. 216, 67–69.

Sundararaghavan, Veera, 2014. Reconstruction of three-dimensional anisotropic microstructures from two-dimensional micrographs imaged on orthogonal planes. Integr. Mater. Manufact. Innov. 3 (1), 19.

Sutton, Michael A, Li, N, Joy, DC, Reynolds, Anthony P, Li, Xiaodong, 2007. Scanning electron microscopy for quantitative small and large deformation measurements part I: SEM imaging at magnifications from 200 to 10,000. Exp. Mech. 47 (6), 775–787.

Suzuki, Atsuo, Iri, Masao, 1986. Approximation of a tessellation of the plane by a voronoi diagram. J. Oper. Res. Soc. Japan. 29 (1), 69–97.

Trinchet-Almaguer, D., Pérez-Rosés, H., 2007. Algorithm for solving the generalized inverse voronoi problem. Rev. Cubana Cien. Inform. 1 (4), 58–71.

Yaghoobi, Mohammadreza, Ganesan, Sriram, Sundar, Srihari, Lakshmanan, Aaditya, Rudraraju, Shiva, Allison, John E, Sundararaghavan, Veera, 2019. PRISMS-plasticity: An open-source crystal plasticity finite element software. Comput. Mater. Sci. 169, 109078.

Zeghadi, A, N'guyen, F, Forest, S, Gourgues, A-F, Bouaziz, O, 2007. Ensemble averaging stress–strain fields in polycrystalline aggregates with a constrained surface microstructure–part 1: Anisotropic elastic behaviour. Phil. Mag. 87 (8–9), 1425–1446.